The Role of Mold Electromagnetic Stirring in the Dissipation of Superheat during the Continuous Casting of Billets

Zhao Zhang, Menghuai Wu, Haijie Zhang, Andreas Ludwig, and Abdellah Kharicha*

A two-phase solidification model coupling mold electromagnetic stirring (M-EMS) is used to investigate the initial solidification in the mold region of billet continuous casting. One novelty of this numerical study is to quantify how the M-EMS induces primary and secondary flows, interacting with the jet flows coming from the submerged entry nozzle, and how those flows further influence the dissipation of superheat and the initial solidification. The role of the M-EMS in speeding up the superheat dissipation in the mold region, known from previous studies and casting practices, is quantitatively verified. Additionally, some new knowledge regarding the M-EMS is found. The total heat transfer rate from the strand surface to the water-cooled copper mold is not affected by the M-EMS; with the M-EMS, the superheat effect on the solid growth can only be detected in the out-of-the-mold region, while the shell growth inside the mold region is quite independent of the superheat; a strong M-EMS tends to accelerate the growth of the solid shell in the mold region, but delays its growth in the secondary cooling zones. The aforementioned new findings may only be valid for the case of the current billet casting, to be confirmed for other casting formats/parameters.

1. Introduction

During the continuous casting of billets, a steel melt is poured into a water-cooled copper mold with a certain superheat. Superheat is defined as the sensible energy contained in the melt above the liquidus,[1] but it is often simply referred to as the temperature difference above the liquidus. It is generally recognized that casting with a low superheat is beneficial for minimizing centerline segregation by facilitating the formation of a central equiaxed zone.[2–4]

Z. Zhang, M. Wu, H. Zhang, A. Ludwig, A. Kharicha
Simulation and Modelling of Metallurgical Processes
Department of Metallurgy
Montanuniversitaet Leoben
Franz-Josef-Str. 18, 8700 Leoben, Austria
E-mail: menghuai.wu@unileoben.ac.at

The ORCID identification number(s) for the author(s) of this article can be found under https://doi.org/10.1002/srin.202200065.

DOI: 10.1002/srin.202200065

Mold electromagnetic stirring (M-EMS), as an additional engineering measure, has been widely used to optimize fluid flow and heat transfer, and hence to control as-cast structures and macrosegregation.[5–11] The swirling flow generated by M-EMS can effectively speed up the superheat dissipation in the mold region, and as a consequence, the equiaxed nuclei originating from crystal fragmentation or heterogeneous nucleation can survive the superheat and form the central equiaxed zone.[12,13]

Due to the harsh environment and high cost of field experiments, numerical modeling has become an effective tool for investigating transport behavior with M-EMS. Yu et al.[14] developed a mathematical model to investigate the effect of M-EMS on the flow field, temperature profile, and inclusion trajectories in round billet continuous casting. They found that the core temperature was dramatically reduced with M-EMS. An et al.[15] proposed a 3D mathematical model to study the effect of current intensity and frequency on fluid flow, and the simulation results also indicated that M-EMS tends to accelerate superheat dissipation. However, solidification was ignored in the above studies.

Ren et al.[16] developed a mathematical model to investigate the influence of M-EMS on fluid flow, heat transfer, and solidification in round bloom continuous casting. They found that M-EMS prevents the superheated jet from moving downward and thus accelerates superheat dissipation in the mold region. Li et al.[17] proposed a coupled magnetohydrodynamics (MHD) model to study the electromagnetic field, fluid flow, and solidification with M-EMS in bloom continuous casting. The maximum melt swirling flow velocity was found to be remarkably decreased when considering solidification. Meanwhile, the M-EMS-induced swirling flow was beneficial for preventing the superheated melt from moving down into the liquid core below. Trindade et al.[18] used a coupled numerical model to study the fluid flow, temperature distribution, and solidification of round billet continuous casting under M-EMS. They found that M-EMS tends to decrease the temperature in the strand center and locally reduce the shell thickness due to the increase in the tangential velocity close to the wall. However, common drawbacks of the previous models are as follows: 1) they used a relatively rough mixture-based model to study the solidification characteristics. The solid shell is simply calculated based on the lever rule, which omits some important characteristic features, i.e., the columnar tip growth velocity and the flow-solidification interaction in the mushy zone; 2) the flow-EMS coupling is simplified. On one hand, the solid shell, which has a higher electrical conductivity than the liquid melt, is ignored when calculating the Lorentz force. On the other hand, the effect of melt flow on the Lorentz force is ignored. The original Lorentz force should be reduced under the effect of a rotating melt flow. Ignorance of this modification would overestimate the melt flow. Dong et al.[19] developed a magnetohydrodynamic model to investigate the effect of fluid flow on the magnetic field, induced current, and electromagnetic force. They found that the flow field in the mold has a certain influence on the magnetic field, the effect of fluid flow in M-EMS calculation should not be ignored. However, the mixture solidification model used in their study failed to treat the columnar tip growth and the flow-solidification interaction in the mushy zone accurately.

In this study, a two-phase columnar solidification model is used to investigate the superheat dissipation in billet continuous casting under the effect of M-EMS. The evolution of the solid shell of the strand is considered using the two-phase model as columnar dendritic structures, whose front is dynamically tracked. The flow-solidification interaction in the mushy zone, and its effect on the formation of macrosegregation are considered. Importantly, a proper coupling scheme between the electromagnetic field and the melt flow is used to treat the flow-EMS integration, i.e., the tangential velocity of the melt that follows the rotational magnetic field would reduce the Lorentz force. Additionally, state-dependent electrical conductivity is used for liquid melts and solid shells, i.e., the solid shell is electrically more conductive than the liquid melt. Parameter studies were performed by varying the superheat and M-EMS electric current intensity.

2. Model Description

2.1. Basis Assumptions

A two-phase columnar solidification model is presented to study the initial solidification of the billet strands. The governing equations of the solidification model, are summarized in **Table 1**, and details of the model are described elsewhere.[20–23] The main features/assumptions are given below. 1) Two phases are defined: liquid melt (ℓ) and solid columnar dendrites (c). Their volume fractions (f_ℓ, f_c) sum up to one. The velocity of the liquid melt is obtained by solving the corresponding Navier–Stokes equations, and the motion of the columnar phase is set constant (equal to the casting speed); 2) The columnar dendrites are assumed to develop directly from the strand surface. The position of the columnar tip front is explicitly treated according to the Lipton–Glicksman–Kurz model[24]; 3) Since the magnetic Reynolds used in the current study is relatively large (0.0463). In addition, the liquid rotating angular speed ($\omega_\ell = 4.27\ \mathrm{rad\ s^{-1}}$) is about 22% of the magnetic rotating angular speed ($\omega_\mathrm{B} = 18.85\ \mathrm{rad\ s^{-1}}$). Thus, it is necessary to consider the effect of melt flow on the electromagnetic force. The time-averaged rotational electromagnetic force ($\vec{F}_\mathrm{L}$) is calculated based on the Maxwell equations. To consider the interaction between the melt flow and the magnetic field, the electromagnetic force is modified by considering the relative motion between the rotation magnetic field and the tangential velocity of the melt, $\vec{F}'_\mathrm{L} = \vec{F}_\mathrm{L}(1 - \vec{u}_\theta/(2\pi f \cdot r))$, where $\vec{u}_\theta$ is the tangential component of the melt velocity, f is the M-EMS frequency and r is the radial coordinate. $\vec{F}'_\mathrm{L}$ is implemented in the model; 4) Volume-averaged concentrations of the liquid melt (c_ℓ) and solid columnar dendrites (c_c) are calculated. Macrosegregation is characterized by the segregation index, $c_\mathrm{mix}^\mathrm{index} = (c_\mathrm{mix} - c_0)\times 100/c_0$, in which c_0 is the initial concentration and c_mix is the mixture concentration, $c_\mathrm{mix} = (f_\ell\ \rho_\ell\ c_\ell + f_c\ \rho_c\ c_c)/(f_\ell\ \rho_\ell + f_c\ \rho_c)$; and 5) Solidification shrinkage is ignored, and the thermal-solutal convection of melt is modeled with the Boussinesq approach.

2.2. Geometry and Boundary Conditions

Figure 1a reveals the geometrical configuration of billet continuous casting with M-EMS. The dimensions and relative positions between the mold and M-EMS are shown in Figure 1b. The distribution of simulated and measured magnetic flux density along the axis-line of mold in the absence of strand are displayed in Figure 1c. A satisfactory simulation-experiment agreement is obtained. The stirrer is fed using a three-phase alternative current (AC) with a frequency of 3 Hz. The current intensity is set to 430 A for the reference case. The casting format is 195 mm × 195 mm, referring to an industrial process. Since the current study focuses on the initial state of solidification, i.e., the formation of a solid shell in the mold region and solidification in the first and second cooling regions, the entire calculation domain (length of the strand) is limited to only 3 m from the meniscus. A 3D calculation (3 m long) requires 7 days on a high-performance cluster (2.6 GHz, 28 cores). For commercial reasons, the composition of the industrial alloy is omitted, but it is simplified as an equivalent binary alloy with a nominal composition of Fe–0.53 wt.%C. The pouring temperature of the reference case is set to 1708.15 K. Parameter studies will be performed by varying the pouring temperature (1698.15–1718.15 K) and M-EMS intensity (200–600 A). A five-port submerged entry nozzle (SEN) is applied, with M-EMS located at the bottom of the mold. On-site measurements of the magnetic flux density along the axis on the continuous casting machine of an empty mold at room temperature were made, which were used to validate the electromagnetic calculation (ANSYS-Maxwell). A satisfactory agreement was obtained between the calculation and measurement. A constant heat transfer coefficient was applied in the mold region to calculate the heat extraction from the strand surface to the copper mold. The heat flux thermal boundary conditions are used in the secondary cooling zones and for commercial reasons, the values are omitted. The strand-mold interface is regarded as electrically isolating. The material properties are listed in **Table 2**.

2.3. Numerical Procedure

Electromagnetic-computational fluid dynamics (EM-CFD) iteration was conducted on two commercial software programs, namely ANSYS-Maxwell and ANSYS-Fluent. The ANSYS Fluent add-on MHD module provides a coupled calculation scheme, but the original magnetic field ($\vec{B}_0$) must be provided

Table 1. Governing equations of the two-phase columnar solidification model.

Governing equations		Symbols
1. Mass conservations		f_l, f_c, volume fraction of liquid and columnar phases [−]
$\frac{\partial}{\partial t}(f_l\rho_l)+\nabla\cdot(f_l\rho_l\vec{u}_l)=-M_{lc}$	(1)	ρ_l, ρ_c, density of liquid and columnar phases [kg m^{-3}]
$\frac{\partial}{\partial t}(f_c\rho_c)=M_{lc}$	(2)	$\vec{u}_l$, velocity vector of the liquid [m s^{-1}]
$f_\ell+f_c=1$	(3)	M_{lc}, net mass transfer rate [kg m^{-3} s^{-1}]
2. Momentum conservations		$\overline{\overline{\tau}}_l$, stress–strain tensors [kg m^{-1} s^{-1}]
$\frac{\partial}{\partial t}(f_l\rho_l\vec{u}_l)+\nabla\cdot(f_l\rho_l\vec{u}_l\otimes\vec{u}_l)=-f_l\nabla p+\nabla\cdot\overline{\overline{\tau}}_l+f_l\rho_l\vec{g}'_l+f_l\vec{F}_L{}'-\vec{U}_{lc}$	(4)	p, pressure [N m^{-2}]
$\vec{g}'_l=\frac{\rho_l^b(T,c_l)-\rho_l^{ref}}{\rho_l^{ref}}\vec{g}$	(5)	$\vec{g}$, $\vec{g}'_l$, gravity and deduced gravity [m s^{-2}]
$\rho_l^b(T,c_l)=\rho_l^{ref}\cdot\left(1+\beta_T\cdot\left(T^{ref}-T_l\right)+\beta_c\cdot\left(c^{ref}-c_l\right)\right)$	(6)	ρ_l^b, density for buoyancy force [kg m^{-3}]
$\vec{F}_L{}'=\vec{F}_L\left(1-\frac{\vec{u}_\theta}{2\pi f\cdot r}\right)$	(7)	ρ_l^{ref}, reference density [kg m^{-3}]
		T^{ref}, reference temperature [K]
		c^{ref}, reference concentration [−]
		β_T, thermal expansion coefficient [K^{-1}]
		β_c, solutal expansion coefficient [wt%$^{-1}$]
		$\vec{F}_L$, $\vec{F}_L{}'$, Lorentz force and modified Lorentz force [N m^{-3}]
		$\vec{U}_{lc}$, momentum exchange rate [kg m^{-2} s^{-2}]
		$\vec{u}_\theta$, tangential velocity [m s^{-1}]
		f, frequency of the applied current [Hz]
		r, radial coordinate [m]
3. Species conservations		c_l, c_c, species concentration of liquid and columnar phases [−]
$\frac{\partial}{\partial t}(f_l\rho_l c_l)+\nabla\cdot(f_l\rho_l\vec{u}_l c_l)=\nabla\cdot(f_l\rho_l D_l\nabla c_l)-C_{lc}$	(8)	D_l, D_c, diffusion coefficient of liquid and columnar phases [m^2 s^{-1}]
$\frac{\partial}{\partial t}(f_c\rho_c c_c)=\nabla\cdot(f_c\rho_c D_c\nabla c_c)+C_{lc}$	(9)	C_{lc}, species exchange rate [kg m^{-3} s^{-1}]
4. Enthalpy conservations		h_l, h_c, enthalpy of liquid and columnar phases [J kg^{-1}]
$\frac{\partial}{\partial t}(f_l\rho_l h_l)+\nabla\cdot(f_l\rho_l\vec{u}_l h_l)=\nabla\cdot(f_l k_l\nabla\cdot T_l)-Q_{lc}$	(10)	k_l, k_c, thermal conductivity of liquid and columnar phases [W m^{-1} K^{-1}]
$\frac{\partial}{\partial t}(f_c\rho_c h_c)=\nabla\cdot(f_c k_c\nabla\cdot T_c)+Q_{lc}$	(11)	Q_{lc}, energy exchange rate [J m^{-3} s^{-1}]
5. Electromagnetic field		$\vec{B}$, magnetic flux density [T]
$\vec{B}=\mu_0\mu_r\vec{H}$	(12)	$\vec{B}^*$, conjugate magnetic flux density [T]
$\nabla\times\vec{E}=-\frac{\partial\vec{B}}{\partial t}$	(13)	$\vec{H}$, magnetic field intensity [A m^{-1}]
$\vec{J}=\sigma\vec{E}$	(14)	μ_0, magnetic permeability in vacuum [T m A^{-1}]
$\vec{F}_L=\frac{1}{2}R_e\left(\vec{J}\times\vec{B}^*\right)$	(15)	μ_r, relative magnetic permeability [−]
		$\vec{E}$, electric field intensity [V m^{-1}]
		$\vec{J}$, induced current density [A m^{-2}]
		σ, electrical conductivity [Ω^{-1} m^{-1}]
		$\vec{F}_L$, time-averaged Lorentz force [N m^{-3}]
		R_e, the real part of a complex number [−]

either by EM calculation (ANSYS-Maxwell) or experimental measurement. Because of the explicit temporal resolution of $\vec{B}_0$, the time step for the numerical simulation should be very small. The additional calculation of the induced magnetic field ($\vec{b}$) equations and their interaction with the momentum equations and energy equations are computationally costly. Additionally, the add-on MHD module in ANSYS Fluent is not compatible with the Eulerian–Eulerian approach, which is used for the multiphase solidification problem.[25] Thus, another relatively simple but reasonable method was used. First, the time-averaged Lorentz force ($\vec{F}_L$) was calculated using ANSYS-Maxwell with the assumption that the calculation domain is full of stationary melt. Then, $\vec{F}_L$ was interpolated into the mesh system of ANSYS-Fluent, weighted by the corresponding phase volume fraction (melt, columnar), and finally added as a source term to the momentum conservation equation of each phase via user-defined functions (UDFs). To consider the interaction between the melt flow and magnetic field, $\vec{F}_L$ was modified by considering a factor that is related to the relative velocity between the rotational magnetic field and the tangential velocity of the melt (Equation (7)). The calculations of the melt flow, heat transfer and solute transport were coupled in ANSYS-Fluent.

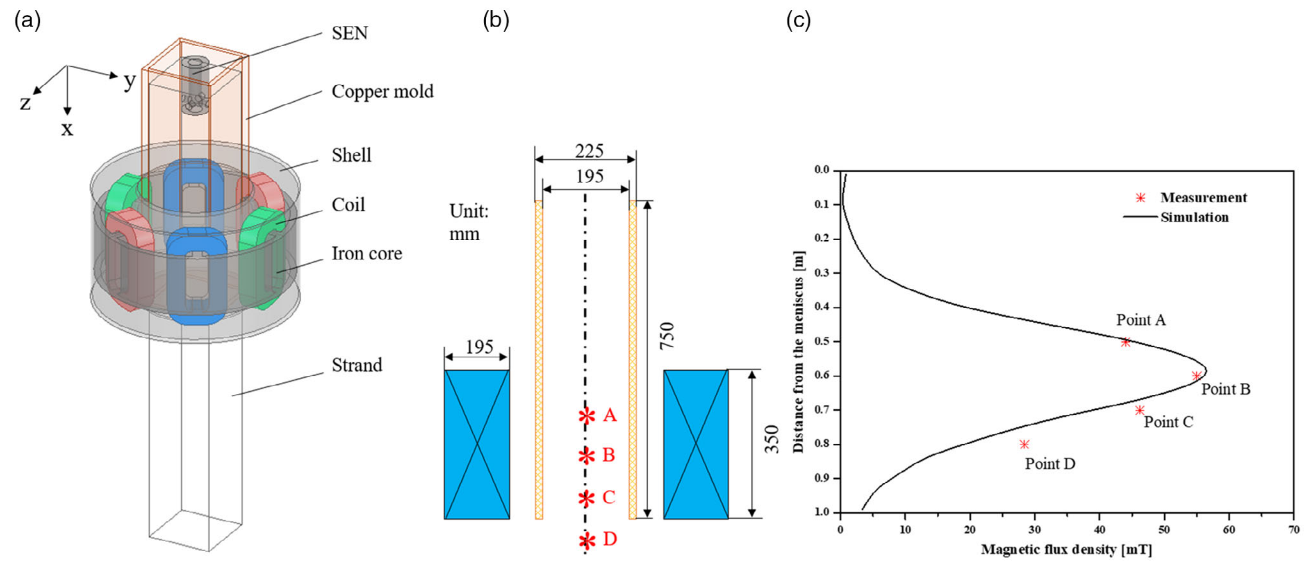

Figure 1. a) Geometrical configuration of billet continuous casting with M-EMS; b) dimensions and relative positions between the mold and M-EMS; c) distributions of simulated and measured magnetic flux density along the axis-line of mold in the absence of strand.

Table 2. Material properties.

Material properties	Symbols	Units	Values
Nominal concentration	c_0	wt.%	0.53
Liquidus temperature	T_L	K	1688.15
Solidus temperature	T_S	K	1593.15
Liquid density	ρ_ℓ	kg m^{-3}	7035.0
Latent heat	L	kJ kg^{-1}	220.0
Specific heat	c_p	J kg^{-1} K^{-1}	800.0
Thermal conductivity	k_ℓ, k_s	W m^{-1} K^{-1}	33.0
Diffusion coefficient in liquid	D_ℓ	m^2 s^{-1}	2.0×10^{-8}
Diffusion coefficient in solid	D_s	m^2 s^{-1}	1.0×10^{-9}
Thermal expansion coefficient of the melt	β_T	K^{-1}	4.5×10^{-5}
Solutal expansion coefficient of the melt	β_C	wt.%$^{-1}$	0.02
Equilibrium partition coefficient of carbon	k	–	0.252
Electric conductivity of strand (melt)	σ_ℓ	S m^{-1}	7.6×10^5
Electric conductivity of strand (solid)	σ_s	S m^{-1}	8.2×10^5
Electric conductivity of copper mold	σ_m	S m^{-1}	3.18×10^7
Primary dendritic arm spacing	λ_1	m	1.85×10^{-4}
Secondary dendritic arm spacing	λ_2	m	4.8×10^{-5}
Viscosity	μ_ℓ	kg m^{-1} s^{-1}	0.006
Gibbs Thomson coefficient	Γ	m K	3.3×10^{-7}
Casting speed	V_c	m min^{-1}	0.8

After the casting reached a quasi-steady state, the profile of the solid shell was exported from ANSYS-Fluent and then imported to ANSYS-Maxwell to recalculate $\vec{F}_L$. The solid shell used a relatively higher electrical conductivity (8.2×10^5 S m^{-1}) than the stationary melt (7.6×10^5 S m^{-1}). The recalculated $\vec{F}_L$ was exported from the ANSYS-Maxwell and then interpolated to ANSYS-Fluent to recalculate the melt flow, heat transfer, and solute transport. When the casting process approaches the quasi-steady state again, the simulation results are analyzed with highlight.

3. Results

3.1. Flow Field

Comparisons of the original Lorentz force and modified Lorentz force are displayed in **Figure 2**. Distributions of the Lorentz force on the central vertical plane of the strand are shown in Figure 2a, and the Lorentz forces on the cross-section plane at the position of the M-EMS center are shown in Figure 2b. Two isolines are plotted to present the solidified shell ($f_c = 0.7$) and columnar solidification front ($f_c = 0.05$). It is clear to see that the two Lorentz forces are basically the same within the solidified shell region where the liquid tangential velocity $\vec{u}_\theta$(Equation (7)) is nearly zero. While in the mushy zone and bulk liquid region, the movement of the liquid melt tends to decrease the Lorentz force correspondingly. Profiles of the Lorentz force along the centerline (Line 1) of the M-EMS center plane are shown in Figure 2c. Two isolines are used to define the different solidification regions (bulk liquid, mushy zone, and solid shell). The M-EMS-induced swirling flow is capable to reduce the original Lorentz force by up to 45.34% at the columnar solidification front (0.072 m to the strand center). It is obvious that ignorance of the modification will overestimate the liquid flow and further influence the heat/mass transfer rate during the billet continuous casting.

Figure 3a shows the velocity contour of the flow pattern. To understand the effect of M-EMS, two cases are compared here, namely, without and with M-EMS. The quarter of the calculation domain is cut vertically in Figure 3a to get a better view of the

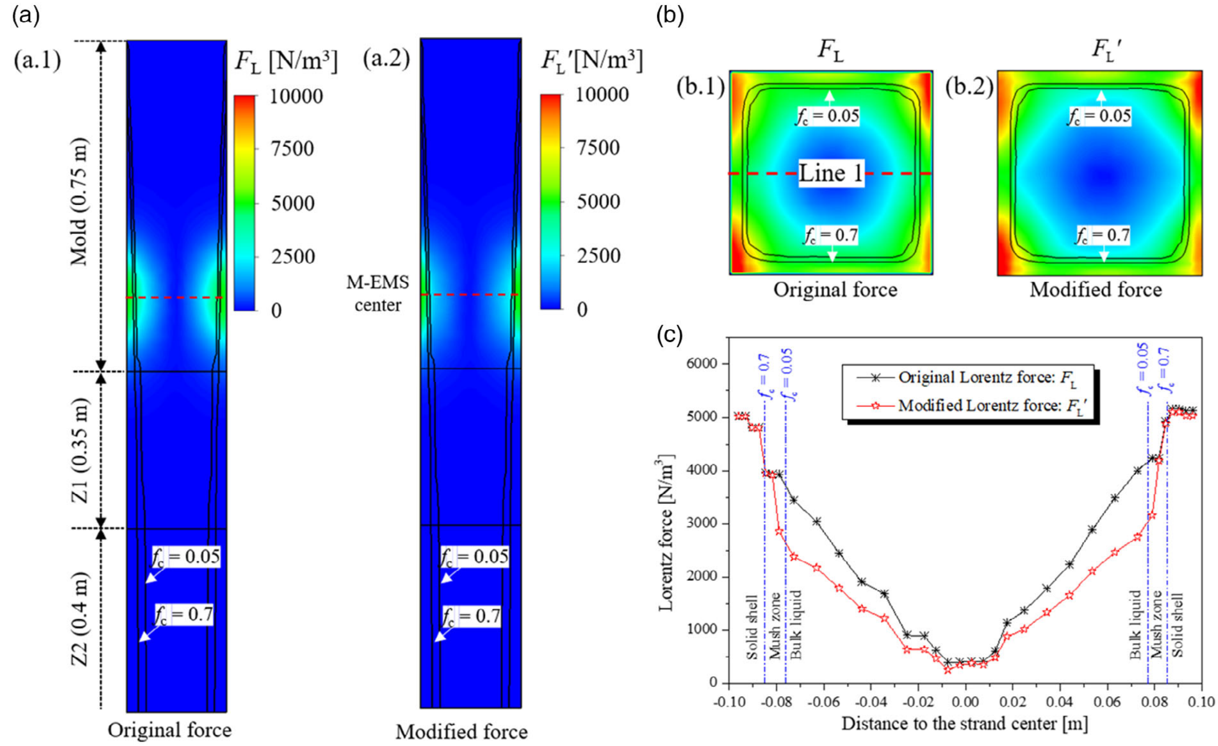

Figure 2. a) Distributions of the Lorentz force on the central vertical plane of the strand overlaid with two isolines to present the solid shell ($f_c = 0.7$) and columnar solidification front ($f_c = 0.05$), a.1) original Lorentz force $\vec{F}_L$; a.2) modified Lorentz force $\vec{F}'_L$; b) Lorentz force on cross-sectional plane at the position of M-EMS center, b.1) original Lorentz force $\vec{F}_L$; b.2) modified Lorentz force $\vec{F}'_L$; c) Lorentz force profiles along the centerline (Line 1) of (b).

inner information of the billet strand. Zoom-views of the flow pattern at the upper part of the mold region are shown in Figure 3b, zoom-views of the flow pattern at the lower part of the mold region are displayed in Figure 3c. In addition, the flow patterns on horizontal sections at the position of the M-EMS center are also shown in Figure 3c. Two isolines are also plotted to present the solidified shell ($f_c = 0.7$) and columnar solidification front ($f_c = 0.05$). The analysis area is limited to 1.5 meters from the meniscus, covering the mold region and two secondary cooling zones (Z1 and Z2). The jet flow coming from the side port of the SEN impinges on the strand wall and is split into two opposite streams. The upper stream is confined by the meniscus, forming an upper vortex that plays an important role in preventing the solidification of the meniscus. M-EMS has a small effect on this vortex (Figure 3b). However, the flow patterns below the SEN are strikingly different between the two cases. For the case without M-EMS, the impinging jet coming from the bottom port of the SEN flows straight down, as does the melt near the solidification front. To conserve these two downward flows, an upward flow forms in the middle radius section of the strand (Figure 3b,c)). Thus, the left and right recirculation loops are created on the half-vertical plane of the strand. For the case with M-EMS, the melt at the center of the strand (M-EMS region) will be brought to the solidification front and move upward/downward. Figure 3d shows the 3D streamline of the melt. Without M-EMS, the flow pattern is relatively simple, i.e., most of the melt coming from the SEN flows downward and returns back to the mold region along the mid-radius region. With M-EMS, a typical swirling flow is generated by the stirrer. The melt above the stirrer spirally flows upward to the upper part of the mold region along the solidification front and then returns to the M-EMS region along the centerline of the strand, forming a so-called upper recirculation loop. In contrast, the melt below the stirrer spirally flows downward along the solidification front and then returns to the stirrer region along the centerline of the strand, and a so-called lower recirculation loop is formed. This form of the flow pattern favors the promotion of superheat dissipation and concentration homogeneity.

3.2. Temperature Field

Figure 4a shows the temperature field for two cases, without and with M-EMS. The simulation results on vertical symmetrical planes are shown in Figure 4a.1, and the simulation results on horizontal sections at the position of the M-EMS center are shown in Figure 4a.2. The superheat region is highlighted and enclosed by the isotherm of $T = 1688.15$ K, which refers to the liquidus of the steel with an initial composition of c_0. It is obvious that, when M-EMS is not applied, the superheat region is extended to far below the mold region along the billet centerline. When M-EMS is applied, the superheat region is confined only in the mold region. Due to the intensive heat transfer rate from strand surface to water-cooled mold, more superheats could be dissipated in this area (Figure 4a.2). The temperature profile

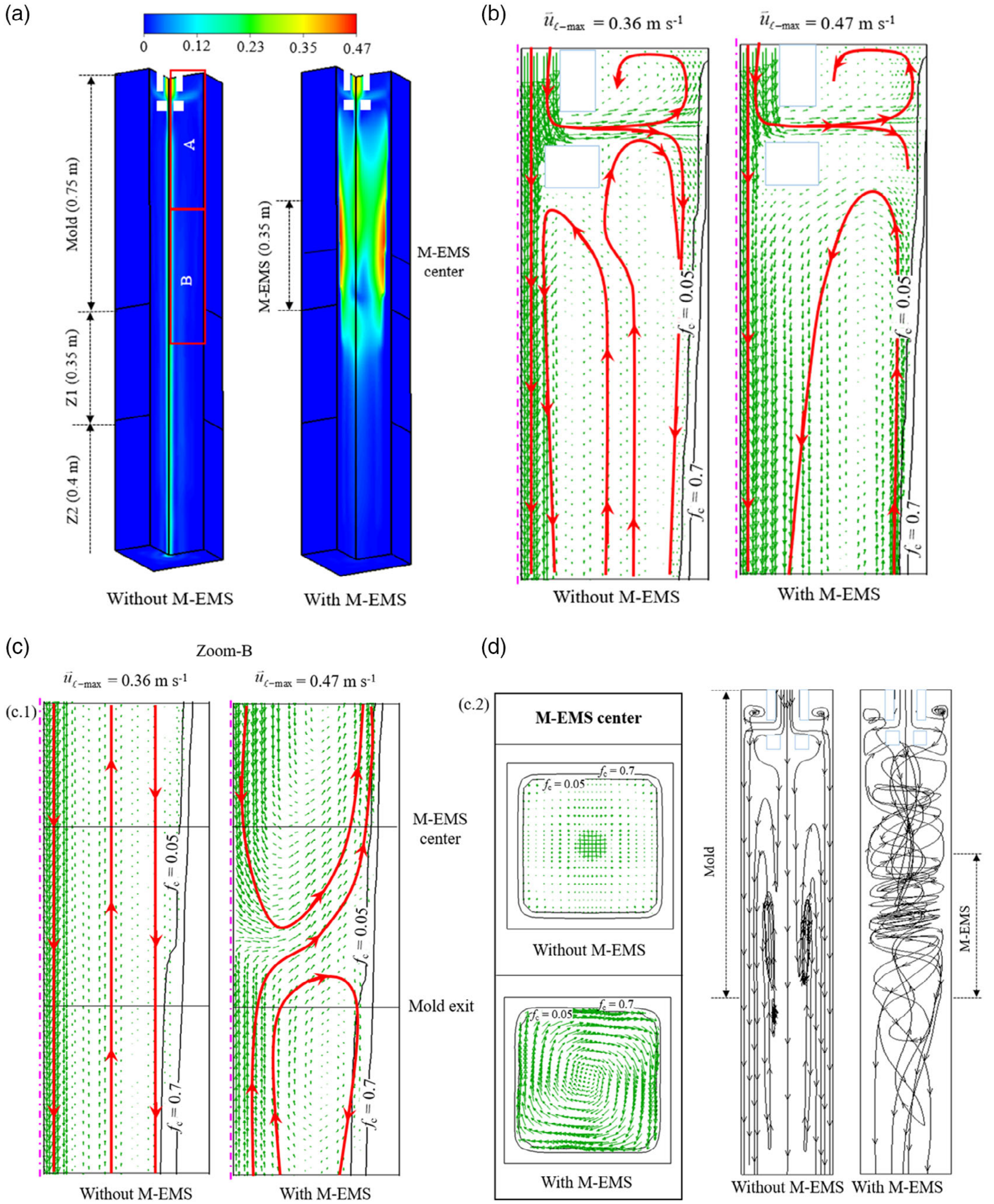

Figure 3. Comparison of the velocity fields for two cases: without and with M-EMS. a) Velocity contour of the flow pattern; b) zoom-view of the flow pattern at the upper part of the mold (Zone-A); c) zoom-view of the flow pattern at the lower part of the mold (Zone-B), c.1) on vertical symmetrical planes; c.2) on horizontal sections at the position of the M-EMS center; d) 3D streamline of the melt.

along the axis line of the strand is presented in Figure 4b. The melt enters the mold through SEN at the same temperature (1708.15 K) for both simulation cases. It then suddenly decreases at 0.2 m below the meniscus. For the case without M-EMS, the temperature decreases from 1708.15 to 1705.12 K. This phenomenon can be easily explained by its flow pattern. The left recirculation loop generated on the half vertical plane continuously brings the cooler melt (still superheated) to the strand center (Figure 3b), while the impact region is limited to a small area below the SEN. Therefore, the temperature curve fluctuates slightly as the distance from the meniscus increases. The temperature is 1705.18 K at the mold exit with a tiny change in the secondary cooling zone. For the case with M-EMS, the temperature decreases from 1708.15 to 1700.96 K at 0.2 m below the meniscus, which is attributed to the M-EMS-induced upper recirculation loop, which carries the cooler melt from the solidification front to the center of the strand. The impact area of the upper recirculation loop extends almost to the entire mold

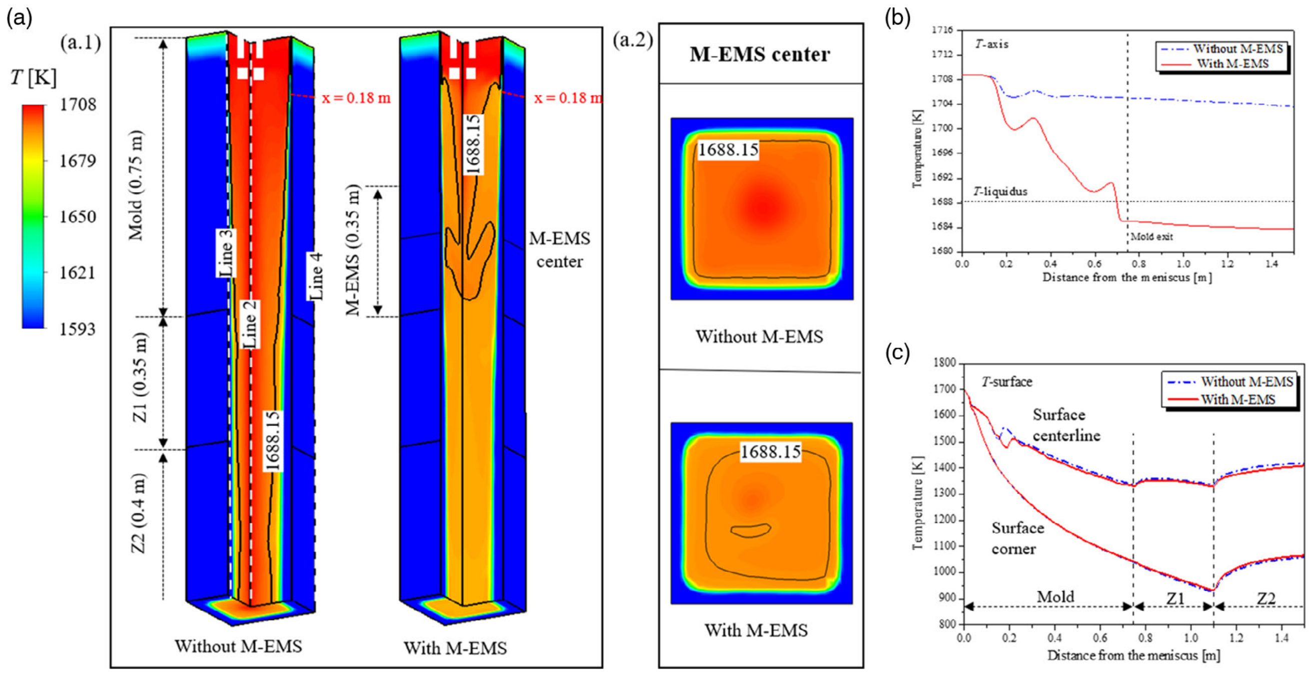

Figure 4. Comparison of the temperature distributions for two cases: without and with M-EMS. a) Contours of the temperature field overlaid with the isotherm of 1688.15 K, which refers to the liquidus of the steel with an initial composition c_0, a.1) vertical symmetrical planes, a.2) horizontal sections at the position of the M-EMS center; b) temperature profiles along the axis-line of the strand (Line 2); c) temperature profiles along the centerline (Line 3) and corner (Line 4) of a strand surface.

region; thus, the temperature decreases continuously as the distance to the meniscus increases. The temperature reaches 1685.03 K (≈3 K below the liquidus) at the mold exit (Figure 4b). Only a tiny change in the temperature is found in the secondary cooling zone. This region, a state of undercooling, is beneficial for the survival of crystal fragments created by M-EMS-induced fragmentation of columnar dendrites. Temperature profiles along the centerline of a strand surface are shown in Figure 4c. Below the side port of SEN, the two curves of the surface centerline show opposite trends at 0.18 m below the meniscus, which is mainly caused by the different flow patterns of the two cases. For the case without M-EMS, the rise in temperature is attributed to the right recirculation loop, which carries the high-temperature melt to the solidification front. The cooler melt is spirally brought to the upper mold region along the solidification front by the upper recirculation loop when M-EMS is applied. Another role of the upper recirculation loop is to inhibit the downward flow of the melt coming from the side port of the SEN. These two effects will subsequently reduce the wall temperature of the strand. After this point, the wall temperature is slightly higher for the case without M-EMS. The temperature profiles along the corner of a strand surface of the two cases are also compared in Figure 4c. It seems that M-EMS-induced flow has an ignorable effect on the temperature distribution at the outer surface corner. The two curves almost overlap with one another. Interestingly, the global heat transfer rate from the strand surface to the water-cooled copper mold seems unlikely to be affected by M-EMS. By integrating the heat flux over the total strand surface in the mold region, the value of the integrated heat flow rate is 503905.5 W for the case without *M*-EMS, and 503588.1 W for the case with M-EMS. The heat flux from the strand to the mold depends on the strand (solid shell) surface temperature. As the M-EMS does not influence the strand surface temperature (Figure 4c), it does not influence the total heat transfer rate from the strand surface to the water-cooled copper mold. The M-EMS-induced flow is beneficial for the temperature homogenization in the liquid core, but the temperature in the shell, especially at the shell surface, is rarely influenced by the M-EMS.

3.3. Growth of the Solid Shell/mushy Zone and Formation of Subsurface Macrosegregation

Figure 5a compares the contours of the volume fraction of the solid columnar dendrites (f_c) for the two cases without and with M-EMS, with no obvious difference found between them. Contours of the volume fractions of the solid columnar dendrites on the horizontal section at the position of the mold exit are shown in Figure 5b. It seems that M-EMS tends to inhibit the growth of the mushy zone at mold exit. The evolutions of the shell thickness and the mushy zone thickness (the distance between the two isolines $f_c = 0.7$ and 0.05) along the casting direction for the two cases are compared in Figure 5c. The positions of the mold exit and the M-EMS center are also marked in Figure 5c. It seems that an M-EMS-induced flow slightly promotes the growth of the solid shell/mushy zone above the M-EMS center but inhibits their growth below the M-EMS center. The reason is that the M-EMS-induced upper recirculation loop (Figure 3b) drives the cooler melt upward along the

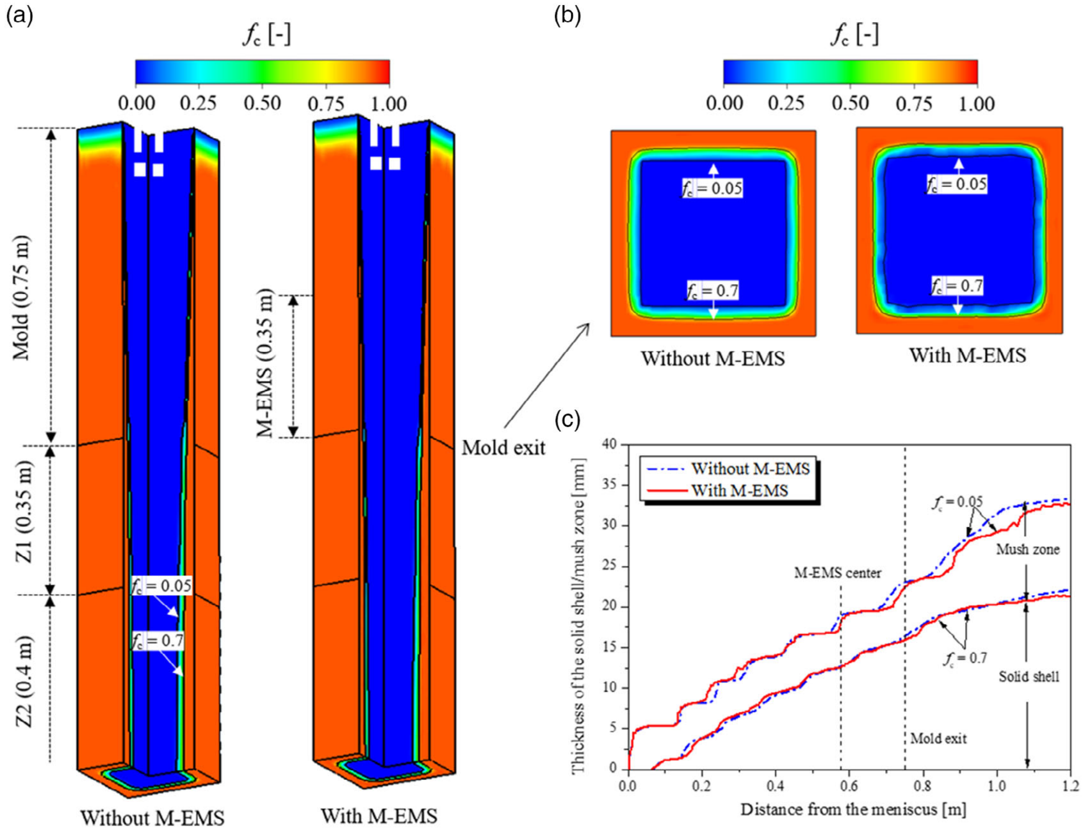

Figure 5. Comparison of the thickness of the solid shell and mushy zone of the two cases: without/with M-EMS. a) Contours of the volume fraction of solid columnar dendrites on vertical symmetrical planes; b) contours of the volume fraction of solid columnar dendrites on horizontal sections at the position of mold exit; c) thickness of the solid shell/mushy zone along the casting direction.

solidification front. This type of flow intends to reduce the temperature near the solidification front, which is beneficial for the growth of the solid shell/mushy zone. Conversely, the M-EMS-induced lower recirculation loop (Figure 3c) continuously brings the hotter melt from the stand center to the solidification front and delays the growth of the solid shell/mushy zone. Although a qualitative trend can be observed, the influence of M-EMS-induced flows on the evolution of the solid shell (quantitative results) is not as obvious in the current case with an applied electric current intensity of 430 A for the M-EMS. The thickness of the solid shell at the mold exit is 16.423 mm without M-EMS, and the value is 15.981 mm with M-EMS. The M-EMS-induced flow only reduces the shell thickness by 0.442 mm.

Figure 6a shows the contours of the macrosegregation index for the two cases: without/with M-EMS. Section views of the macrosegregation on the M-EMS center plane are displayed in Figure 6b, and profiles of the macrosegregation along the diagonal line (Line 5) of this plane are shown in Figure 6c. For the case without M-EMS, the macrosegregation is negligible, while for the case with M-EMS, due to the “solute washing” effect, the M-EMS-induced horizontal swirling flow penetrates the mushy zone and sweeps out the solute enriched melt to the bulk liquid. Subsurface negative segregation is formed, with the worst negative segregation appearing near the corner of the strand. It should be noted that the negative segregation is fixed in the solidified shell (inside of the isoline $f_c = 0.7$). Thus, the degree of negative segregation will not change as solidification progresses. Meanwhile, the solute is slightly enriched in the bulk region (Figure 6c). This solute enrichment cannot be considered to be macrosegregation, since this solute-enriched melt will solidify later to form the center as-cast structure (mostly equiaxed), and the final segregation profile will change correspondingly. This is further discussed in §5.

4. Parameter Studies

To further investigate the interplay between M-EMS and superheat, parameter studies were also performed by varying the superheat (10, 15, 20, 25, 30 K) and the M-EMS electric current intensity (200, 300, 430, 500, 600 A).

4.1. Superheat

Figure 7 shows the influence of the superheat (10–30 K) on the temperature distribution in the mold and secondary cooling regions. The electric current intensity is kept constant (430 A). The temperature contours on vertical symmetrical planes are shown in Figure 7a. The superheated zone is marked with an isotherm of 1688.15 K, which corresponds to the liquidus of the steel with an initial composition of c_0. It is obvious that

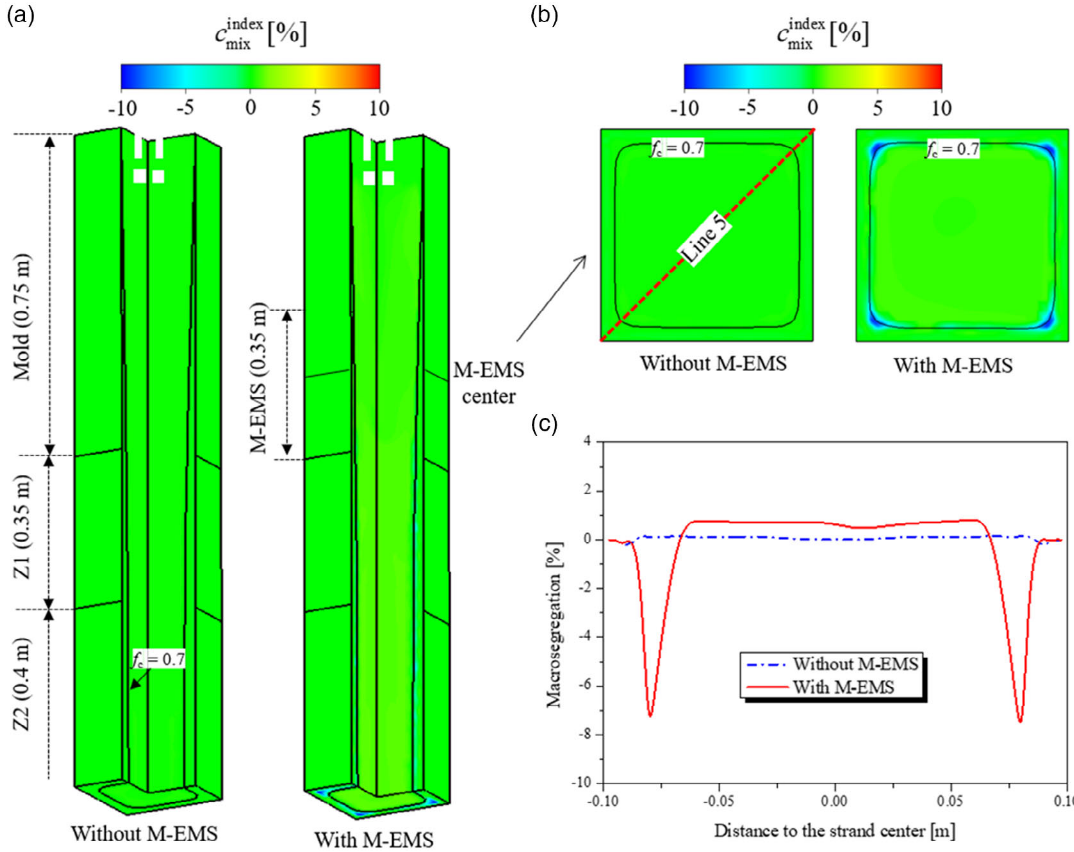

Figure 6. Comparison of the macrosegregation between the two cases: without/with M-EMS. a) Contours of the macrosegregation index on vertical symmetry planes and b) on horizontal sections at the position of the M-EMS center; c) macrosegregation profiles along the diagonal line (Line 5) of (b).

the superheated area gradually expands to the entire mold region with increased superheating. When the superheat is 10 K, the upper recirculation loop (Figure 3b) generated by the M-EMS can easily cool the liquid temperature below the liquidus. The superheated region, starting from the SEN, can only extend to two-thirds of the mold region and is only limited to the center of the strand. When the superheat is 30 K, the superheated region extends to almost the entire mold region. The extended superheated region does not favor the growth of solid shells and the heterogeneous nucleation of equiaxed crystals. Furthermore, the crystal fragments will be remelted/destructed when they are brought into this superheated area.

Figure 7b depicts the temperature profiles along the axis-line of the strand. The temperatures of the melt are almost constant (but different between the five cases with different superheats) in the SEN region and then decrease sharply as they enter the M-EMS region. The superheated areas are mainly confined in the mold region (Figure 7a). The temperatures at the mold exit of the five cases are all below the liquidus temperature, leaving the liquid core out of the mold region undercooled. The temperature differences between the five cases are not as obvious in the secondary cooling zones. The temperature is 1684.16 K at the mold exit and 1684.11 K at 1.27 m below the meniscus of the first case ($\Delta T = 10$ K), while the value is 1684.71 K at the mold exit and 1684.59 K at 1.27 m below the meniscus of the last case ($\Delta T = 30$ K). The temperature difference is only ≈0.55 K at the mold exit and 0.48 K at 1.27 m below the meniscus between the two cases. This means that the influence of the superheat on the temperature distribution in the center of the strand is quite weak in the secondary cooling zones. The temperature profiles along the centerline of a strand surface are shown in Figure 7c. It is interesting to find that the superheat seems to have a tiny effect on the surface temperature in the mold region, but it can significantly raise the surface temperature in the secondary cooling zones with an increased superheat. The reason is that M-EMS tends to homogenize the temperature in the liquid core of the strand, the increased thermal energy is transferred to the sensible energy and stored in the solid shell and liquid phase (near the solidification front) in the secondary cooling zones as increasing the superheat. The temperature is 1391.42 K in the first case ($\Delta T = 10$ K), and 1426.78 K in the last case ($\Delta T = 30$ K) at 1.27 m below the meniscus, for a difference of 35.36 K. The higher surface temperature of the last case ($\Delta T = 30$ K) will delay the growth of the solid shell/mushy zone in the secondary cooling zones.

Figure 8 shows the effect of superheat on the evolution of the solid shell and the mushy zone. The contours of f_c on the vertical symmetry planes are shown in Figure 8a. It is obvious that the region of the solid shell/mushy zone is compressed by increasing the superheat. Quantitative analyses are conducted to reveal the thickness of the solid shell/mushy zone along the casting

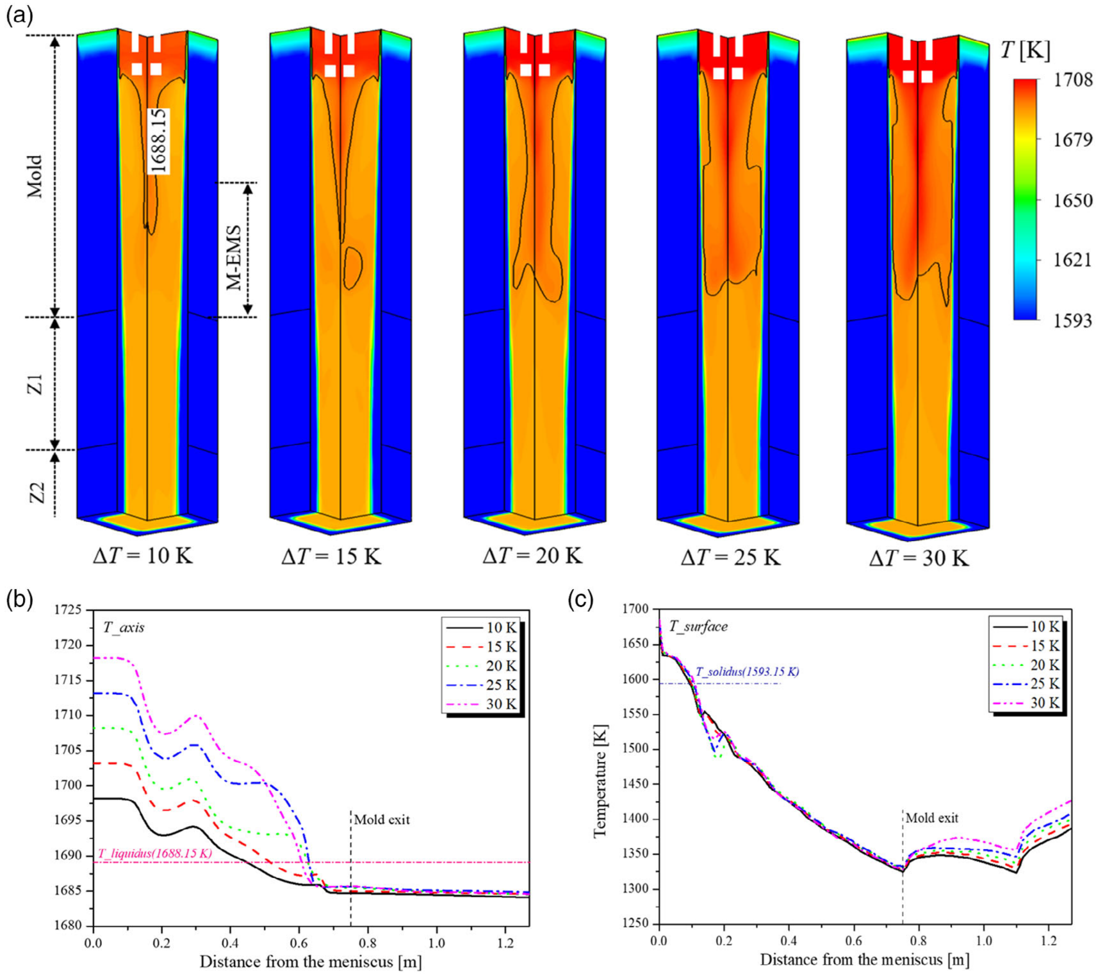

Figure 7. Influence of the superheat (10–30 K) on the temperature distribution. M-EMS is kept constant (430 A). a) Temperature contours on the vertical symmetry planes; b) profiles of the temperature along the axis-line of the strand; c) profiles of the temperature along the centerline of a strand surface.

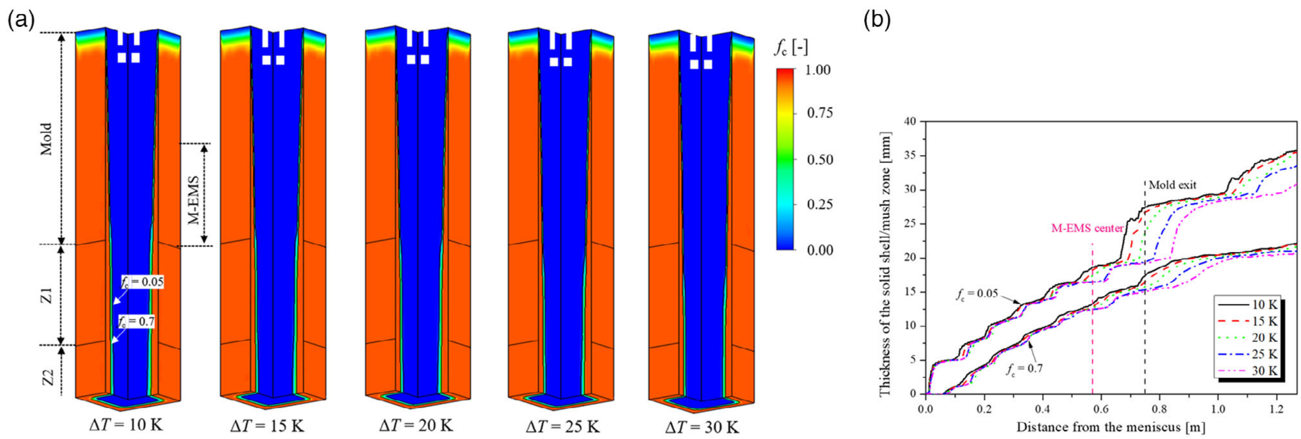

Figure 8. Effect of the superheat (10–30 K) on the evolution of the solid shell and mushy zone. a) Contours of f_c on the vertical symmetry planes; b) thickness of the solid shell/mushy zone along the casting direction.

direction in Figure 8b. As mentioned before, the superheat has a tiny effect on the surface temperature in the mold region. Thus, no large difference in the thickness of the solid shell/mushy zone can be found in this area. However, starting from the secondary cooling zones, the enormous surface temperature distinctions of the five cases will definitely influence the growth of the solid shell/mushy zone. The thickness of the solid shell at the mold exit is 17.38 mm in the first case ($\Delta T = 10$ K) and 15.14 mm in the last case ($\Delta T = 30$ K). Increasing the superheat by 20 K will reduce the solid shell thickness by 2.24 mm at the mold exit. It is, therefore, concluded that the higher superheat is not beneficial for the growth of the solid shell, especially in the secondary cooling zones. A similar conclusion also applies to the growth of the mushy zone; the columnar solidification front ($f_c = 0.05$) is compressed by increasing the superheat.

4.2. Electric Current Intensity

Figure 9 presents the influence of the electric current intensity (200–600 A) of M-EMS on the temperature distribution in the mold and secondary cooling regions. The superheat is kept constant (20 K). Figure 9a displays the contours of the temperature on the vertical symmetry planes. It can be seen that the superheated region is shifted upward with an increasing electric current intensity of M-EMS. This is conducive to accelerating the dissipation of the superheat.

Figure 9b shows the temperature profiles along the axis-line of the strand. For the case where the electric current intensity is equal to 200 A, the relatively weak stirring intensity is not sufficient to decrease the axis temperature below the liquidus temperature at the mold exit. The superheated region, therefore, extends to the secondary cooling zones until the position 1 m below the meniscus. For the other four cases (300–600 A), the stirring intensity is powerful enough to decrease the axis temperature below the liquidus temperature at the mold exit and leave the liquid core out of the mold region undercooled. When the current intensity is sufficiently large (>430 A), a further increase in the electric current intensity will no longer influence the core temperature in the secondary cooling zones. The temperature profiles along the centerline of a strand surface are shown in Figure 9c. It seems that increasing the electric current intensity is prone to decreasing the surface temperature in the mold region, but it is prone to increase the surface temperature in the secondary cooling zones. This phenomenon can also be explained by the flow patterns shown in Figure 2b,c. The M-EMS-induced upper recirculation loop, which tends to bring the cooler melt to the upper part of the mold region along

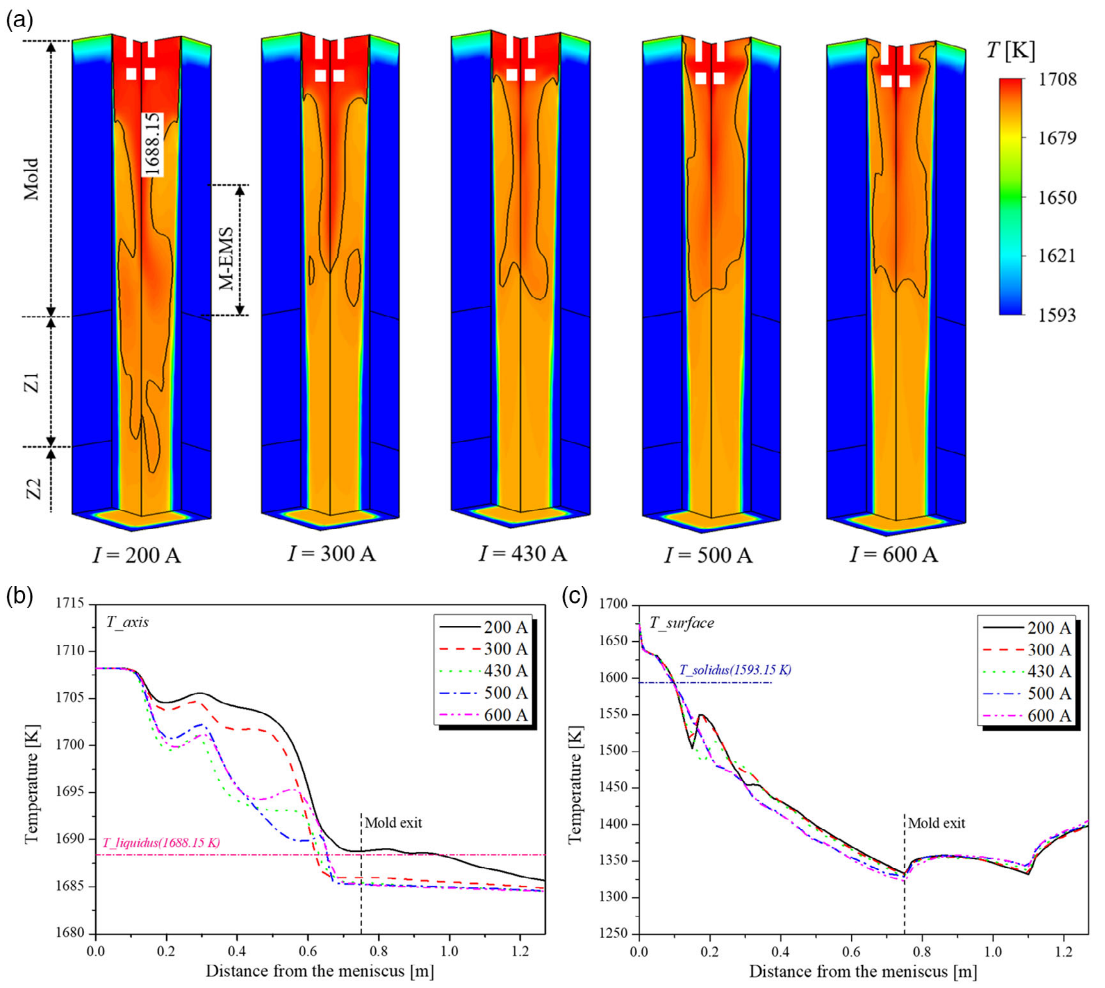

Figure 9. Influence of the electric current intensity (200–600 A) of M-EMS on the temperature distribution. The superheat is kept constant (20 K). a) Contours of the temperature on the vertical symmetry planes; b) profiles of the temperature along the axis-line of the strand; c) profiles of the temperature along the centerline of a strand surface.

the solidification front, will be enhanced with an increasing electric current intensity. This will cause a drop in the surface temperature in the mold region. Similarly, the enhanced lower recirculation loop tends to raise the surface temperature in the secondary cooling zone by increasing the electric current intensity.

Figure 10 displays the effect of the electric current intensity (200–600 A) of M-EMS on the evolution of the solid shell/mushy zone. The contours of f_c on the vertical symmetry planes are shown in Figure 10a. For a quantitative comparison, the thickness of the solid shell/mushy zone along the casting direction of the five cases is plotted in Figure 10b. By increasing the electric current intensity, the lower surface temperature tends to facilitate the growth of the solid shell/mushy zone in the mold region (this is more obvious when the current intensity is larger than 430 A). It will further be beneficial for the fragmentation of solid columnar dendrites and increases the number of equiaxed grains. In contrast, the higher surface temperature tends to delay the growth of the solid shell/mushy zone in the secondary cooling zones (this is more obvious when the current intensity is larger than 430 A).

5. Discussion

In this work, a two-phase (liquid, columnar) solidification model is used to investigate the superheat dissipation in billet continuous casting under the effect of M-EMS. Superheat dissipation is an important message for analyzing the growth of solid shells and hence further affects the possible formation of subsurface macrosegregation. However, one must state that the formation/growth, migration and remelting/destruction of equiaxed crystals play an important role during the continuous casting of billet strands. It is true that to understand the formation of the final as-cast structure and macrosegregation in the billet, a three-phase mixed columnar-equiaxed model is needed. This was done by the authors in a previous paper.[26] Demonstratively, the calculated as-cast structure is shown in **Figure 11**, and satisfactory agreement with the field experiment was obtained. The columnar zone, mixed zone, and equiaxed zone of the calculated as-cast structure are distinguished by two isolines of equiaxed grain envelope: $f_e^{env} = 1.0$ and $f_e^{env} = 0.17$. $f_e^{env} = f_e/f_{si}$, where f_e is the volume fraction of equiaxed crystals, and f_{si} is the volume ratio of solid dendrites to equiaxed grain envelope ($f_{si} = 0.3$ in

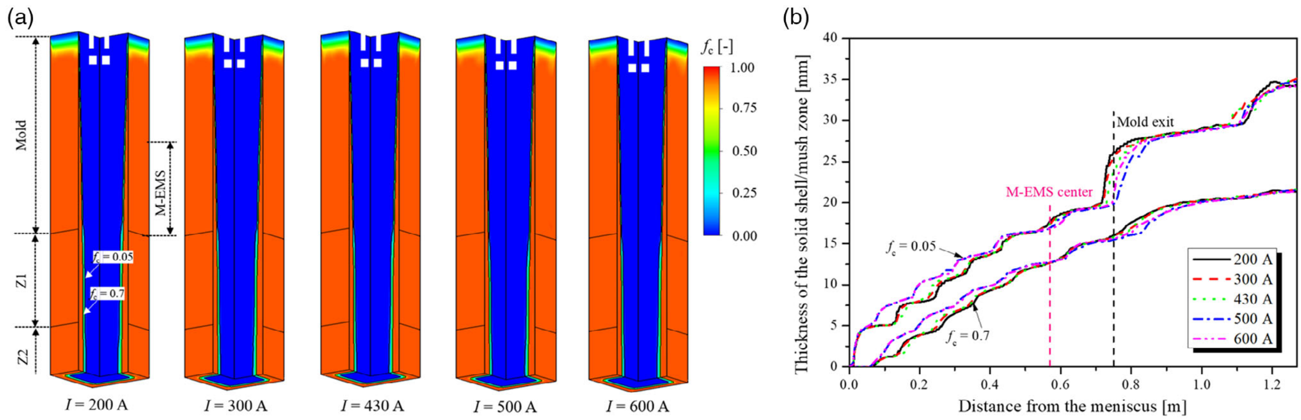

Figure 10. Effect of the electric current intensity (200–600 A) of M-EMS on the evolution of the solid shell and mushy zone. a) Contours of f_c on vertical symmetry planes; b) thickness of the solid shell/mushy zone along the casting direction.

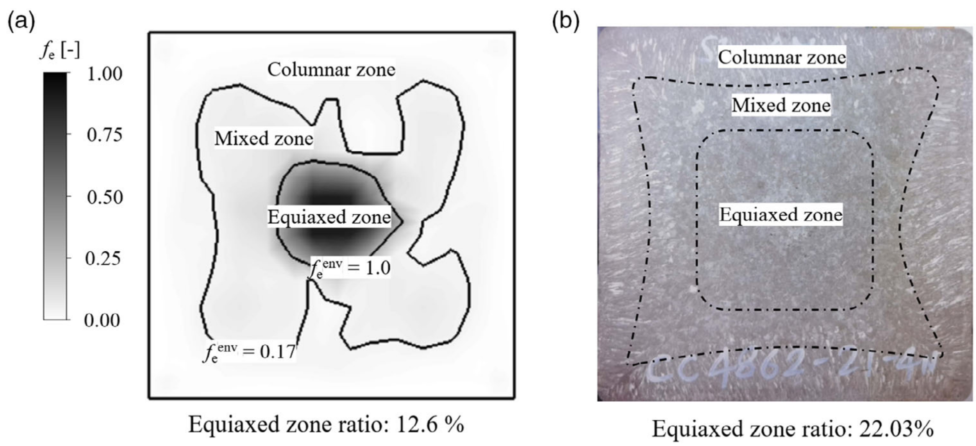

Figure 11. a) Calculated distribution of equiaxed crystals overlaid with two isolines of the equiaxed grain envelope: $f_e^{env} = 1.0$ and $f_e^{env} = 0.17$; b) as-cast structure. Reproduced with permission.[26] Copyright 2022, Elsevier.

this calculation). Two mechanisms (heterogeneous nucleation[20] and fragmentation of dendrites[27]) contributed to the source of equiaxed crystals, wherein the initial inoculant number density (n_{in}^{0}) is set as 1×10^{9}, and the fragmentation coefficient (γ) is set as 3.0×10^{-5}.

The reason why the current study is only limited to the two-phase model is due to the calculation cost. A 3D calculation of a full length of casting (≈12 m) with the three-phase model requires 45 days on a high-performance cluster (2.6 GHz, 28 cores), while a 3D calculation for the initial solidification of a part of the strand (3 m long) with the two-phase model only needs 7 days of calculation time. It is not wise to conduct parameter studies on such a time-consuming case (three-phase, 12 m). The calculations based on the two-phase model can also effectively reflect the effect of M-EMS on the superheat dissipation during the continuous casting of billets. **Figure 12**a depicts the temperature fields of the two cases (without/with M-EMS) by using the two-phase model in a 3 m calculation domain. Figure 12b shows the temperature fields of the two cases (without/with M-EMS) by using the three-phase model in a 12 m calculation domain. The same conclusion could be drawn by analyzing the simulation results of the two simulation models: the role of M-EMS in the dissipation of superheat during the continuous casting of billets is to speed up the superheat dissipation in the mold region, leaving the liquid core out of the mold region greatly undercooled.

6. Conclusion

A two-phase solidification model was used to investigate the effect of M-EMS on the dissipation of superheat in the mold region of billet continuous casting. A proper coupling scheme between the electromagnetic field and the melt flow is used to treat the flow-EMS interaction. The electric conductivity of the material is treated as state-dependent, i.e., the liquid melt and solid shell have different electric conductivities. Parameter studies were also performed by varying the superheat and the electric current intensity of M-EMS. The following new findings were obtained. 1) The M-EMS-induced horizontal swirling flow speeds up the superheat dissipation in the mold region, leaving the liquid core out of the mold region largely undercooled. However, the total heat transfer rate from the strand surface to the water-cooled copper mold is not affected by M-EMS; 2) The growth of the solid shell is not evidently influenced by M-EMS. Subsurface

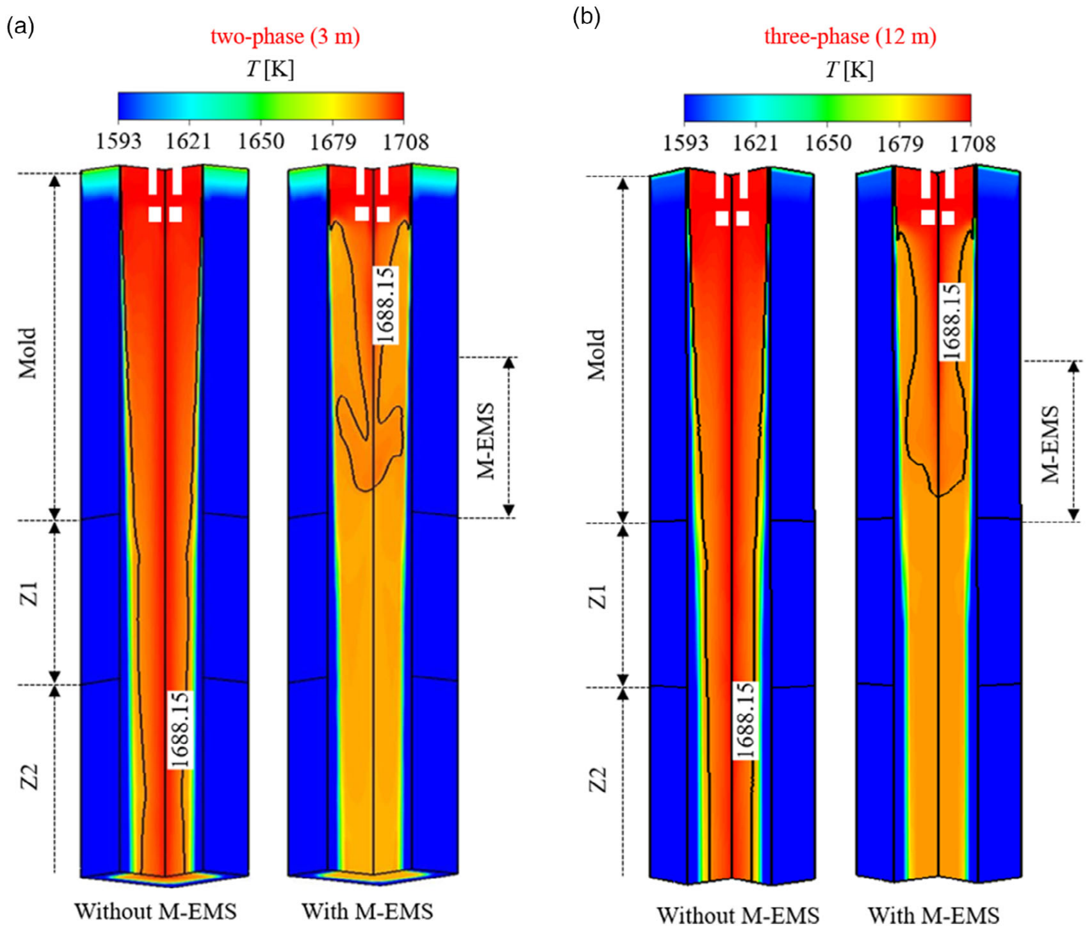

Figure 12. Comparison between the two models, i.e., two-phase columnar solidification model versus three-phase mixed columnar-equiaxed solidification model. a) Temperature fields of the two cases (with/without M-EMS) by using the two-phase model in a 3 m calculation domain; b) temperature fields of the two cases (with/without M-EMS) by using the three-phase model in a 12 m calculation domain.

negative segregation near the strand corner is formed due to the M-EMS-induced swirling flow; 3) With the M-EMS, the effect of the melt superheating on the growth of the solid shell/mushy zone can only be detected in the out-of-the-mold region (the larger the superheat is, the slower the shell growth), while the shell growth inside the mold region is minorly influenced by the superheat; and 4) A strong M-EMS with a large electric current intensity tends to accelerate the growth of the solid shell/mushy zone in the mold region but delay the growth of the solid shell/mushy zone in the secondary cooling zones.

The aforementioned findings might conflict with some existing knowledge and may only be valid for the current casting format/parameters, to be confirmed for other casting formats/parameters of different alloys.

Acknowledgements

The authors acknowledge the financial support from the Austria Research Promotion Agency (FFG) through the Bridge 1 project (No. 868070) as well as the technical support of the industrial partner Primetals Technologies Austria GmbH.

Conflict of Interest

The authors declare no conflict of interest.

Data Availability Statement

The data that support the findings of this study are available from the corresponding author upon reasonable request.

Keywords

continuous casting, electromagnetic stirring, solid shell growth, superheat dissipation

Received: January 24, 2022
Revised: June 26, 2022
Published online:

[1] X. Huang, B. G. Thomas, F. M. Najjar, *Metall. Mater. Trans. B* **1992**, *23*, 339.
[2] S. K. Choudhary, S. Ganguly, *ISIJ Int.* **2007**, *47*, 1759.
[3] S. K. Choudhary, S. Ganguly, A. Sengupta, V. Sharma, *J. Mater. Process. Technol.* **2017**, *243*, 312.
[4] S. Kunstreich, *Rev. Metall.* **2003**, *100*, 1043.
[5] N. A. Shah, J. J. Moore, *Iron Steelmaker* **1982**, *9*, 31.
[6] N. A. Shah, J. J. Moore, *Iron Steelmaker* **1982**, *9*, 42.
[7] B. Z. Ren, D. F. Chen, H. D. Wang, M. J. Long, Z. W. Han, *Ironmaking Steelmaking* **2015**, *42*, 401.
[8] B. X. Wang, W. Chen, Y. Chen, Y. P. Feng, *Ironmaking Steelmaking* **2015**, *42*, 63.
[9] Y. B. Yin, J. M. Zhang, Q. P. Dong, Q. H. Zhou, *Ironmaking Steelmaking* **2019**, *46*, 855.
[10] N. Genma, T. Soejima, T. Saito, M. Kimura, Y. Kaihara, H. Fukumoto, K. Ayata, *ISIJ Int.* **1989**, *29*, 1056.
[11] Q. Fang, H. Zhang, J. H. Wang, C. Liu, H. W. Ni, *Metall. Mater. Trans. B* **2020**, *51*, 1705.
[12] K. Ayata, T. Mori, T. Fujimoto, T. Ohnishi, I. Wakasugi, *Trans. Iron Steel Inst. Jpn.* **1984**, *24*, 931.
[13] Z. G. Yang, B. Wang, X. F. Zhang, Y. T. Wang, H. B. Dong, Q. Liu, *J. Iron Steel Res. Int.* **2014**, *21*, 1095.
[14] H. Q. Yu, M. Y. Zhu, *Ironmaking Steelmaking* **2012**, *39*, 574.
[15] H. H. An, Y. P. Bao, M. Wang, L. H. Zhao, *Metall. Res. Technol.* **2018**, *115*, 103.
[16] B. Z. Ren, D. F. Chen, H. D. Wang, M. J. Long, *Steel Res. Int.* **2015**, *86*, 1104.
[17] S. X. Li, P. Lan, H. Y. Tang, Z. P. Tie, J. Q. Zhang, *Steel Res. Int.* **2018**, *89*, 1800071.
[18] L. B. Trindade, J. E. A. Nadalon, A. C. Contini, R. C. Barroso, *Steel Res. Int.* **2017**, *88*, 1600319.
[19] Q. P. Dong, J. M. Zhang, Q. Liu, Y. B. Yin, *Steel Res. Int.* **2017**, *88*, 1700067.
[20] M. Wu, A. Ludwig, *Metall. Mater. Trans. A* **2006**, *37*, 1613.
[21] M. Wu, A. Ludwig, A. Kharicha, *Metals* **2019**, *9*, 229.
[22] M. Wu, A. Ludwig, A. Kharicha, *Appl. Math. Model.* **2017**, *41*, 102.
[23] J. Li, M. Wu, J. Hao, A. Ludwig, *Comput. Mater. Sci.* **2012**, *55*, 407.
[24] J. Lipton, M. E. Glicksman, W. Kurz, *Mater. Sci. Eng.* **1984**, *65*, 57.
[25] H. J. Zhang, M. Wu, Z. Zhang, A. Ludwig, A. Kharicha, A. Rónaföldi, A. Roósz, Z. Veres, M. Svéda, *Metall. Mater. Trans. B* **2022**, 1.
[26] Z. Zhang, M. Wu, H. J. Zhang, S. Hahn, F. Wimmer, A. Ludwig, A. Kharicha, *J. Mater. Process. Technol.* **2022**, *301*, 117434.
[27] Y. J. Zheng, M. Wu, A. Kharicha, A. Ludwig, *Model. Simul. Mater. Sci. Eng.* **2018**, *26*, 015004.